AGU PUBLICATIONS

Geophysical Research Letters

RESEARCH LETTER
10.1002/2016GL069914

**Key Points:**
- Solar wind charge exchange efficiency factors for oxygen are provided in the 0.5–0.7 keV range, based on solar wind speed
- Equations are provided to estimate $O^{7+}$, $O^{8+}$, O/H, and the efficiency based on solar wind speed
- Oxygen charge state abundances affect magnetosheath X-ray flux more strongly than the O/H ratio

**Correspondence to:**
I. C. Whittaker,
iw47@le.ac.uk

**Citation:**
Whittaker, I. C., and S. Sembay (2016), A comparison of empirical and experimental $O^{7+}$, $O^{8+}$, and O/H values, with applications to terrestrial solar wind charge exchange, *Geophys. Res. Lett.*, *43*, 7328–7337, doi:10.1002/2016GL069914.

Received 7 JUN 2016
Accepted 29 JUN 2016
Accepted article online 5 JUL 2016
Published online 22 JUL 2016



# A comparison of empirical and experimental $O^{7+}$, $O^{8+}$, and O/H values, with applications to terrestrial solar wind charge exchange

**Ian C. Whittaker**[1] **and Steve Sembay**[1]

[1] Department of Physics and Astronomy, University of Leicester, Leicester, United Kingdom

**Abstract** Solar wind charge exchange occurs at Earth between the neutral planetary exosphere and highly charged ions of the solar wind. The main challenge in predicting the resultant photon flux in the X-ray energy bands is due to the interaction efficiency, known as the $\alpha$ value. This study produces experimental $\alpha$ values at the Earth, for oxygen emission in the range of 0.5–0.7 keV. Thirteen years of data from the Advanced Composition Explorer are examined, comparing $O^{7+}$ and $O^{8+}$ abundances, as well as O/H to other solar wind parameters allowing all parameters in the $\alpha_{O^{7,8+}}$ calculation to be estimated based on solar wind velocity. Finally, a table is produced for a range of solar wind speeds giving average $O^{7+}$ and $O^{8+}$ abundances, O/H, and $\alpha_{O^{7,8+}}$ values.

## 1. Introduction

At the Earth, the primary solar wind variables are the proton number density and velocity to produce properties such as the dynamic pressure. Observations of heavy ions in the solar wind composition can be used for purposes such as determining the origin and evolution of the solar wind from the corona [e.g., *Geiss et al.*, 1995; *Tracy et al.*, 2015]; however, the highly charged heavy ions in the solar wind are also important in charge exchange interactions. Solar wind charge exchange (SWCX) is a useful tool for observing how the solar wind interacts with a planetary magnetic system and has been observed in planetary exospheres [e.g., *Holmström et al.*, 2001; *Dennerl*, 2008; *Carter et al.*, 2010; *Ishikawa et al.*, 2013], the Moon [*Collier et al.*, 2014] and comets [e.g., *Lisse et al.*, 1996, 2005].

The SWCX process occurs when a highly ionized heavy ion in the solar wind interacts with a cool neutral, resulting in an electron transfer to the ion at a high-energy state. The energized electron then decays in energy state emitting a photon. X-ray photons emitted from this process in the near-Earth environment are concentrated in the magnetosheath and can be used for magnetospheric imaging [*Collier et al.*, 2012] and magnetopause modeling [e.g., *Collier et al.*, 2005; *Ogasawara et al.*, 2013]. The main limitation with SWCX modeling is the accuracy and availability of heavy ion charge state abundances in the solar wind [e.g., *Kuntz et al.*, 2015; *Whittaker et al.*, 2016]. The equation for calculating X-ray flux due to SWCX is shown in equation (1) [*Cravens*, 2000].

$$P_X = \eta_H \eta_{SW} v_{av} \alpha \tag{1}$$

where $P_X$ = emissivity (eV cm$^{-3}$ s$^{-1}$)

$\eta_{SW}$ = solar wind proton number density (cm$^{-3}$)

$\eta_H$ = neutral hydrogen number density (cm$^{-3}$)

$\alpha$ = scale factor based on cross-sections heavy ion abundances (eV cm$^2$)

$$v_{av} = \sqrt{v_{sw}^2 + \frac{3k_B T}{m_p}} \quad (\mathrm{cms}^{-1}).$$

This study examines the average solar wind variables required and provides estimates based on solar wind velocity, for calculating $\alpha$ in the commonly used 0.5 to 0.7 keV X-ray emission band which contains strong and easily resolved spectral lines for contemporary CCD instruments.

## 2. Methods of Calculating $\alpha$

Empirical models of SWCX generally use a constant value of $\alpha$ covering all species and charge states in the solar wind, such as $1.6 \times 10^{-15}$ [*Schwadron and Cravens*, 2000], $9.4 \times 10^{-16}$ [*Pepino et al.*, 2004] (slow wind), $6 \times 10^{-16}$ [e.g., *Cravens et al.*, 2001; *Robertson and Cravens*, 2003; *Robertson et al.*, 2006], and $3.3 \times 10^{-16}$ eV cm$^2$ [*Pepino et al.*, 2004] (fast wind). These constants combine ionization potentials for species, including C, N, O, Si, S, and Fe, with cross-sectional information and estimated emission probabilities [*Cravens*, 1997]. As such these values contain no direct dependence on the highly variable heavy ion abundances and relative charge states, by definition the fast/slow values of Pepino contains a limited ion dependence. Equation (2) shows the combination of factors to produce an $\alpha$ dependent upon solar wind conditions, where $X$ is the heavy ion species, $q$ the charge state, $E$ the emission line energy, and $\sigma$ the cross section.

$$\alpha_{Xq^+} = \sigma E \left[\frac{X^{q^+}}{X}\right]\left[\frac{X}{H}\right]. \quad (2)$$

To determine the X-ray emission from charge exchange between 0.5 and 0.7 keV, we require $\alpha_{O^{7,8+}}$, as $O^{7+}$ and $O^{8+}$ are the dominant source of charge exchange photons in this energy range. As such we need the oxygen to hydrogen ratio (O/H) and the abundances of both $O^{7+}$ and $O^{8+}$ as a fraction of the total oxygen in the solar wind. The experimentally determined cross-section values are taken from *Bodewits* [2007].

We use the ACE (Advanced Composition Explorer) solar wind monitor to determine the input parameters for calculating $\alpha_{O^{7,8+}}$, hereafter referred to as $\alpha_o$ with units of eV cm$^2$. Errors in the data processing of Solar Wind Ion Composition Spectrometer (SWICS) instruments are covered in Appendix A of *von Steiger and Zurbuchen* [2011]; Figure A2 of this study shows the average statistical uncertainty for specific charge states; $O^{7+}$ shows uncertainty of a few percent, while $O^{8+}$ shows a few tens of percent. For a full review of SWICS see *Gloeckler et al.* [1998]. These results suggest that constraints need to be placed on the ACE data before $\alpha$ is calculated for any line emissions.

The other available source of parameters for calculating $\alpha_o$ comes from *Schwadron and Cravens* [2000]. The slow solar wind values given in this study are $O^{7+}$=0.20, $O^{8+}$=0.07, and O/H=$\frac{1}{1780}$. The fast solar wind values are $O^{7+}$=0.03, $O^{8+}$=0.00, and O/H=$\frac{1}{1550}$. This study uses 810 km/s for fast wind and 442 km/s for slow wind, thus only providing oxygen information for two values on the wide distribution of solar wind velocities.

## 3. The XMM-Newton Case Study Simulations

*Whittaker et al.* [2016] compared model predictions in the 0.5–0.7 keV band to the 19 strongest cases, from an archive of results [*Carter et al.*, 2011], where terrestrial SWCX X-ray emission was evident in XMM-Newton observations. This study used an MHD model with observed solar wind parameters as the input and took an integral emission value through the 3-D datacube around the Earth, created using equation (1). The results showed large variation in the ACE heavy ion data both within and between cases. The study reduced the ACE variation by taking mean charge state abundances for the observation time range and using a modal $\frac{O}{H}$ value of $2 \times 10^{-4}$, improving the correlation quality between observations and modeling.

Figure 1 shows the average $\alpha_o$ value for each case in the *Whittaker et al.* [2016] study with error bars showing the standard deviation of values, combined with the recorded measurement error. Figure 1a uses the original ACE data and takes the median $\alpha_o$ in the near-Earth environment, in the range $0 \le x \le 15\,R_E$, $-18 \le y \le 18\,R_E$, and $-18 \le z \le 18\,R_E$, comprising around one million data values. The red dashed line in Figure 1a indicates the empirical all species $\alpha$ value of $6 \times 10^{-16}$, while the blue dashed line shows the overall median for all 19 cases of $2.39 \times 10^{-16}$. Figure 1b shows the $\alpha_o$ values using a constant $\frac{O}{H}$ and mean charge state abundances for each case. Hence, the variations come from the differences in the MHD model using this method. The median $\alpha_o$ value using these fixed coefficients is $1.70 \times 10^{-16}$. As well as the values calculated in *Whittaker et al.* [2016], we also include the empirical values from *Schwadron and Cravens* [2000]. These average $\alpha_o$ values using fast and slow solar wind oxygen parameters are shown in Figure 1c. These data show the closest clustering to their median value of $3.79 \times 10^{-16}$ as they have the smallest amount of input variables. The only allowable variation is the average collision speed which affects the cross-section interaction values and whether the input solar wind is slow (<500 km/s) or fast (>500 km/s). Figure 1d shows the upstream value calculated $\alpha_o$ using the *Schwadron and Cravens* [2000] inputs and ACE solar wind speed (black stars). The case median of $3.95 \times 10^{-16}$ (blue dashed line) is the median of one data point per time frame. The blue squares in this panel use ACE data

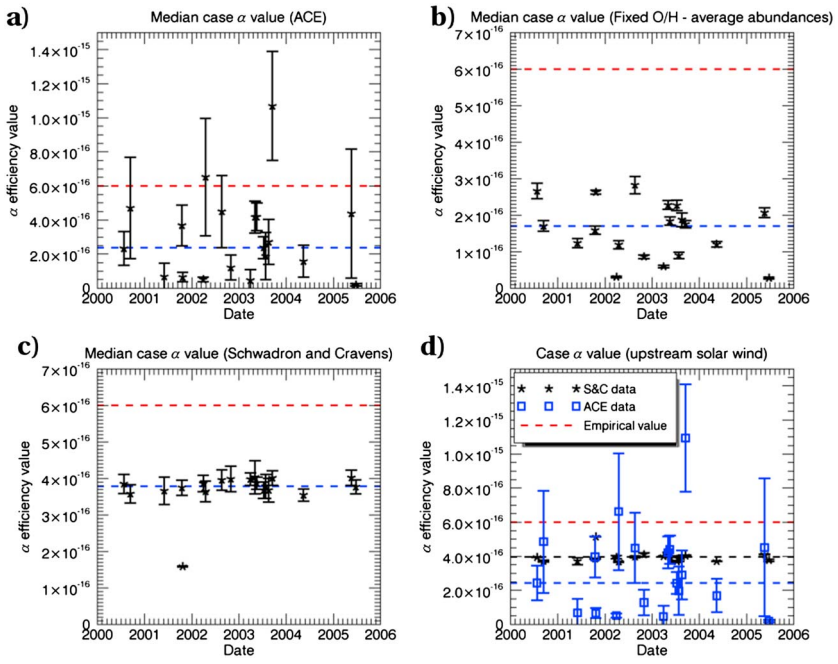


**Figure 1.** The $\alpha_o$ value for XMM-Newton cases examined in *Whittaker et al.* [2016] (see section 3). The all species $\alpha$ empirical value of $6 \times 10^{-16}$ (red dashed line), and the data averages (blue dashed) are shown. (a) The average $\alpha_o$ using ACE abundances. (b) The average $\alpha_o$ using the study fixed abundances. (c) The average $\alpha_o$ using *Schwadron and Cravens* [2000] abundances. (d) The average $\alpha_o$ in the upstream solar wind comprising ACE abundances (blue squares) and empirical values (black stars).

for all the heavy ion information and show a much higher variance in $\alpha_o$. The median of these data (shown as the blue dashed line) is $2.44 \times 10^{-16}$.

As we have large variance in the ACE data, as well as between the different calculated $\alpha_o$, we proceed to investigate the relevant input parameters.

## 4. ACE Data and Probabilities

We have downloaded charge state abundances for $O^{5+}$ to $O^{8+}$, the helium number density, and the He/O ratio between the years of 1998 and 2011 for analysis. The O/H ratio is calculated using equation (3) [*Schwadron and Cravens*, 2000]. The solar wind proton number densities and velocities are supplied from the ACE/Solar Wind Electron, Proton, and Alpha Monitor instrument.

$$\mathrm{O/H} = \frac{N_{\mathrm{He}}}{N_p}\frac{O}{\mathrm{He}}, \tag{3}$$

where $N_p$ and $N_{\mathrm{He}}$ are number densities.

*Schwadron and Cravens* [2000] determine a difference in the oxygen values dependent upon solar wind speed. As the definition of fast and slow solar wind are linked to the origin point on the Sun, with slow solar wind originating in lower latitudes and fast solar wind from the higher latitudes [*McComas et al.*, 1998], the fast/slow definition can also be defined by ion composition. Studies such as *Zurbuchen et al.* [2002] and *von Steiger et al.* [2010] use $O^{7+}/O^{6+}$ as a measure of fast and slow wind. To continue our investigation, we separate out each of the data parameters by solar wind bulk speed.

### 4.1. $\alpha_o$ Values

These 13 years of data at 2 h resolution are combined into $\alpha_o$ values. During this process the SWICS data are examined, with poor-quality data (marked by a quality flag of −1) removed. The $\alpha_o$ values are binned (bin-size = $1 \times 10^{-17}$) and shown as a histogram in Figure 2a. To provide a fit to this distribution, we note the typical lognormal distribution for values based on solar wind parameters [*Burlaga and Lazarus*, 2000], leading to the Gaussian fit shown in purple. The modal upstream $\alpha_o$ from this Gaussian distribution is $3.59 \times 10^{-17}$, while the data have a modal peak at $6 \times 10^{-17}$. This small modal difference arises from the combination of fast and slow

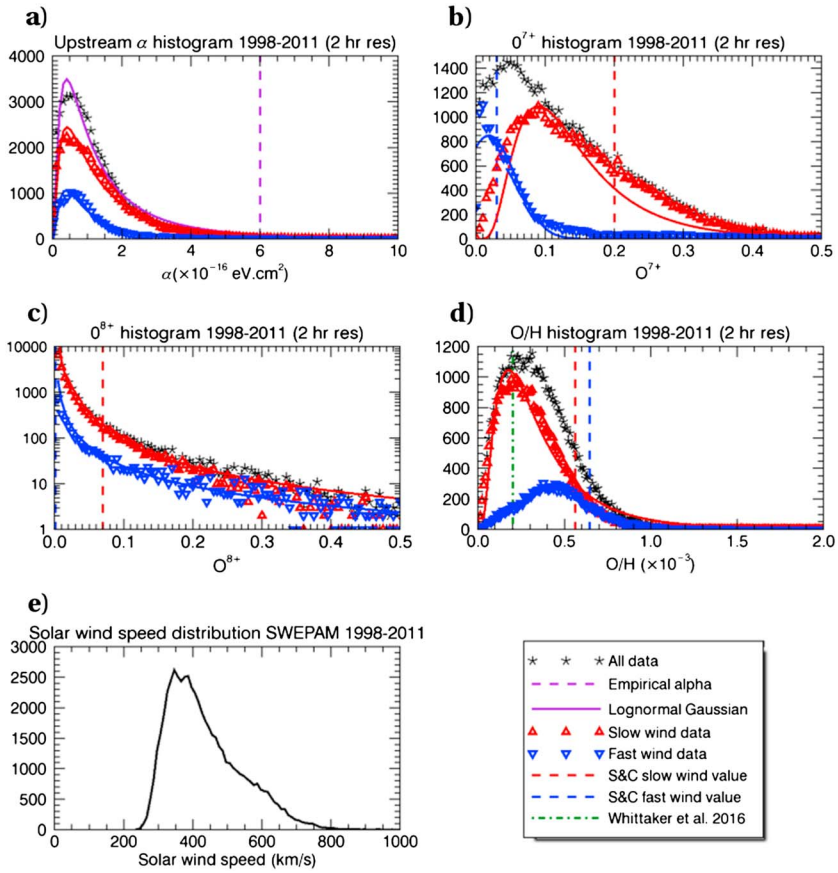


**Figure 2.** ACE data taken over 13 years showing the fast (blue), slow (red), and all (black) solar wind speed oxygen parameters. (a) $\alpha_o$ distributions in the solar wind fitted with lognormal Gaussians. (b) $O^{7+}$ distributions with fitted lognormal Gaussians. (c) $O^{8+}$ distributions with power law fits. (d) O/H distribution in the solar wind. (e) The solar wind speed distribution.

wind paradigms, being modeled by a single function. Equation (4) gives the normalized Gaussian distribution which can be used as a probability distribution to determine the likelihood of calculated $\alpha_o$ values.

$$p = e^{-\left(\frac{\log_{10}\alpha_o + c}{w}\right)^2/2}, \tag{4}$$

where

$$c = 16.445 \pm 0.005 \tag{5}$$

$$w = 0.459 \pm 0.004. \tag{6}$$

The $\alpha_o$ values have been split by solar wind speed, with slow solar wind $\alpha_o$ values shown in red and fast solar wind values shown in blue. The distributions are similar with modal peaks at $3.1 \times 10^{-17}$ (slow wind) and $6.1 \times 10^{-17}$ (fast wind). This difference in magnitude between fast and slow solar wind $\alpha_o$ will become more apparent in the near-Earth environment as the thermal velocity becomes significant.

### 4.2. $O^{7+}$ Values

The $O^{7+}$ abundance values taken from the 13 years of ACE data are shown in Figure 2b. The full histogram (black stars) has a binsize of 0.005 and a peak at an abundance of 0.05. The slow solar wind $O^{7+}$ values are shown in red, with the histogram data shown as triangles, the lognormal Gaussian fit shown as the solid line, and the *Schwadron and Cravens* [2000] value shown as the dashed line. The modal histogram value is 0.089 (8.9%), and the normalized probability distribution is shown in equation (7). The fast $O^{7+}$ values are shown in

blue, with the same line and symbol styles. A standard Gaussian is fit to the data (equation (8)), with a central value of 0.016 (1.6%).

$$p_{v<500\ O^{7+}} = e^{-\left(\frac{\log_{10}O^{7+}+c_s}{w_s}\right)^2/2} \tag{7}$$

$$p_{v>500\ O^{7+}} = e^{-\left(\frac{O^{7+}-c_f}{w_f}\right)^2/2} \tag{8}$$

where

$$c_s = 1.046 \pm 0.006, \quad c_f = 0.016 \pm 0.002 \tag{9}$$

$$w_s = 0.263 \pm 0.004, \quad w_f = 0.039 \pm 0.002. \tag{10}$$

The variation in the peak histogram location between fast and slow wind shows that the full data histogram is clearly a product of at least two separate distributions (Kolmogorov-Smirnov test returns $p < 10^{-8}$).

### 4.3. $O^{8+}$ Values

The $O^{8+}$ data in Figure 2c show a different distribution from both the $\alpha_o$ and the $O^{7+}$ abundance values. The peak of both the slow (red) and fast (blue) solar wind distributions sits in the first bin suggesting the modal $O^{8+}$ abundance is less than 0.5%. Analysis of the full 13 year data set gives the median fast and slow wind $O^{8+}$ abundances of 0.12% and 0.44%, respectively. For comparison the $O^{7+}$ fast and slow medians are 4.4% and 13.7%. The histogram frequency axis is shown on a log scale to better show the power law fit lines. As the power law fit has an asymptote at the zero bin, normalization of the fit equations is impossible. We therefore only supply the power values of −1.77 (slow solar wind) and −1.45 (fast solar wind) for completeness.

### 4.4. O/H Values

Unlike the $\alpha_o$ value and individual charge state abundances, the O/H ratio has been studied in detail. The *Schwadron and Cravens* [2000] O/H values are $5.62 \times 10^{-4}$ (slow wind) and $6.45 \times 10^{-4}$ (fast wind). Ulysses data have previously produced mean O/H values of $4.35 \times 10^{-4}$ (slow wind) and $6.67 \times 10^{-4}$ (fast wind) [*von Steiger et al.*, 2010]. *Lepri et al.* [2013] provided mean values for the O/H ratio at solar maximum and minimum for fast and slow solar wind speeds, ranging from $2.03 \times 10^{-4}$ to $4.76 \times 10^{-4}$ for ACE SWICS data.

The O/H ratio histogram is shown in Figure 2d, with the full data set in black, the slow wind values in red, and the fast wind values in blue. In a similar manner to the $O^{7+}$ data values in Figure 2b we observe that the O/H histogram is composed of two separate distributions. The slow wind peak is $1.65 \times 10^{-4}$, and the fast wind peak is $4.37 \times 10^{-4}$. These values are very close to the *Lepri et al.* [2013] values as they utilize similar data sets. The normalized equations for these O/H wind histograms are shown in equations (11) and (12).

$$p_{v<500\ O/H} = e^{-\left(\frac{\log_{10}O/H+c_{soh}}{w_{soh}}\right)^2/2} \tag{11}$$

$$p_{v>500\ O/H} = e^{-\left(\frac{O/H-c_{foh}}{w_{foh}}\right)^2/2} \tag{12}$$

where

$$c_{soh} = 3.780 \pm 0.003, \quad c_{foh} = 4.37 \pm 0.001 \times 10^{-4} \tag{13}$$

$$w_{soh} = 0.336 \pm 0.003, \quad w_{foh} = 2.02 \pm 0.001 \times 10^{-4}. \tag{14}$$

## 5. Discussion

### 5.1. The $\alpha_o$ and Oxygen Abundance Distributions

Figures 1a–1d show that as expected, the empirical $\alpha$ values are much higher than $\alpha_o$ as they combine all $O^q$, $C^q$, $N^q$, and $Ne^q$ cross sections [*Pepino et al.*, 2004]. Looking at the median upstream values, we see that around the Earth an $\alpha_o$ value of $2 \times 10^{-16}$ is appropriate. Keeping values constant throughout a case reduces the error bars considerably, clearly seen in the upstream solar wind $\alpha_o$ values in Figure 1d. This lack of variation is because the only velocity component which affects the cross sections is the bulk flow of the solar wind.

Whereas in the magnetosheath the temperature addition to velocity, which is a negligible addition in the upstream solar wind, becomes dominant.

The fast and slow solar wind speed fits shown in Figure 2 are dependent on a specific cutoff value of 500 km/s, for completeness we have included the distribution of speeds in Figure 2e. Alternative fitting of each parameter was performed with different speed cutoffs; however, no improvement over the 500 km/s classification was found. As Figure 2 provides normalized Gaussians for $\alpha_o$, $O^{7+}$ and O/H values we can immediately determine any bias in the *Whittaker et al.* [2016] case studies shown in Figure 1. The upstream solar wind $\alpha_o$ median of $2.44 \times 10^{-16}$ using ACE data gives a normalized histogram value of 0.19 using equation (4). In comparison, the upstream $\alpha_o$ value using the *Schwadron and Cravens* [2000] heavy ion data of $3.79 \times 10^{-16}$ returns a normalized frequency of 0.08. As the 19 case studies were taken from the top of a database ranked by how strong the observed SWCX was in XMM-Newton [*Carter et al.*, 2011], it is expected that these cases have a higher than average $\alpha_o$ value. It is worth noting, however, that the average O/H value taken and used in the *Whittaker et al.* [2016] study of $2 \times 10^{-4}$ (green dashed line) is very similar to the slow wind modal peak, indicating that the enhancements seen in XMM-Newton lightcurves are more sensitive to high charge state abundances than changes in the O/H ratio.

When we investigate the oxygen abundances, we can see a clear difference between the fast and slow solar wind. The *Schwadron and Cravens* [2000] values for fast wind are reasonably similar when it comes to the measured $O^{7+}$ and $O^{8+}$, whereas the slow wind measurements are quite different. Interestingly, the width of the Gaussians for fast and slow $O^{7+}$ is approximately the same, indicating that the variance of oxygen is similar. This is in contrast to the different distribution widths of the O/H fits, in agreement with *von Steiger et al.* [2010].

### 5.2. Linking $\alpha_o$ and Oxygen Abundances to Solar Wind Conditions

To determine if fast and slow solar wind have two different oxygen composition types rather than just being a function of speed, we create scatterplots of every applicable data point from the 13 years of ACE data. This not only allows another way of checking the accuracy of any particular data point but also provides a prediction of heavy ion data when no SWICS measurements exist.

Figure 3 contains nine panels showing the scatterplot relations of the three oxygen parameters; Figure 3 (top row) shows the $O^{7+}$, $O^{8+}$, and O/H as a function of solar wind number density, while Figure 3 (middle row) shows the same relations to solar wind bulk speed. As there are 56,074 data points the data have been shown in a 2-D histogram with color indicating the frequency. Figure 3 (top row) shows little correlation between oxygen and solar wind number density. Figure 3 (middle row) comparisons to solar wind speed show better correlations, as expected from Figure 2. In particular, the $O^{7+}$ 2-D histogram in the first panel of Figure 3 (middle row) shows a strong correlation.

As well as the solar wind speed and number density a range of other correlations have been investigated. The most relevant of these are shown in Figure 3 (bottom row). The first panel of Figure 3 (bottom row) shows the relation of the $O^{7+}$ abundance to the $O^{8+}$ abundance in a log-log plot with a dashed red fit line. Due to charge state abundances being frozen into the solar wind in the corona at the same time, it follows that the $O^{7+}$ and $O^{8+}$ abundances should be linked to each other and the freezing in temperature [e.g., *Hundhausen et al.*, 1968; *Hefti et al.*, 2000]. The fit line (given in equation (15)) follows the distribution of points well with a standard deviation of 0.04 from the fit. The correlation begins to break down above an $O^{7+}$ abundance of ~30%, this could be due to poor mass resolution as these will occur at the slowest speeds, or the product of coronal mass ejection (CME) oxygen enhancement.

$$O_{8+} = 0.274 \times O_{7+}^{1.951} \tag{15}$$

The second panel of Figure 3 (bottom row) shows a log-log plot of both $O^{7+}$ and $O^{8+}$ monthly averaged abundances compared to the sunspot number over the 13 years of data. The error bars shown are the standard deviation of the $O^{7+}$ abundance over the month. Error bars are not included for the $O^{8+}$ abundances to improve plot clarity. There is a clear relation indicating that higher abundances are observed at higher activity levels. The increase in solar activity will lead to an increase in coronal mass ejecta, which provide short-term enhancements to the freezing in temperature (for a review see *Zurbuchen and Richardson* [2006]), thereby increasing both $O^{7+}$ and $O^{8+}$, as well as increasing the solar wind density significantly [*Webb and Howard*, 1994]. The fit lines for the $O^{7+}$ abundance (green dashed) and $O^{8+}$ abundance (black dash dotted) have been plotted for completeness.

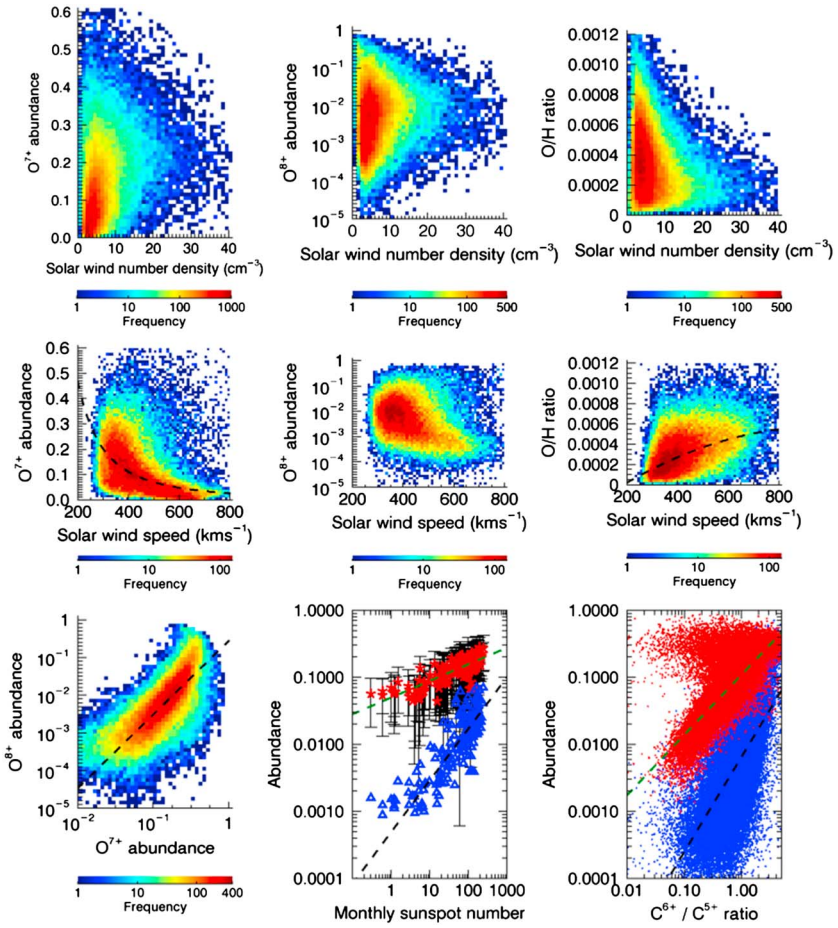


**Figure 3.** Thirteen years of ACE oxygen data compared to the (top row) solar wind number density, (middle row) solar wind bulk flow, and (bottom row) other solar wind parameters. (a) $O^{7+}$ against $n_{sw}$, (b) $O^{8+}$ against $n_{sw}$, (c) O/H against $n_{sw}$. (d) $O^{7+}$ against $v_{sw}$, a power law fit is included (black) (e) $O^{8+}$ against $v_{sw}$, (f) O/H against $v_{sw}$, a polynomial fit line is included (black). (g) $O^{7+}$ against $O^{8+}$, a power law fit is shown (black), (h) $O^{7+}$ (red) and $O^{8+}$ (blue) scatter points as a function of sunspot number, (i) $O^{7+}$ (red) and $O^{8+}$ (blue) scatter points as a function of $\frac{C^{6+}}{C^{5+}}$.

The third panel of Figure 3 (bototm row) shows the scatterplot data of the abundances with the $C^{6+}/C^{5+}$ ratio. The $C^{6+}/C^{5+}$ ratio is part of the condition used in *von Steiger et al.* [2010] to determine the difference between slow and fast solar wind. The increase in carbon ionization should also link to an increase in oxygen ionization due to both being dependent on the coronal freeze in temperature, and the plot shows this to be true. The $O^{8+}$ data are shown in blue (black dash-dotted fit line), while the $O^{7+}$ data are in red (green dashed fit line). The $O^{7+}$ abundance points above 20% which show no relation to the $C^{6+}/C^{5+}$ ratio could be either erroneous data points or CME-enhanced abundances, where the carbon ionization is not affected. Fit lines for both abundance types are plotted for completeness.

Using the results in Figure 3, we can produce a set of $\alpha_o$ values for a range of conditions. While the strongest correlations of the abundances are with monthly sunspot values or the $C^{6+}/C^{5+}$ ratio, neither of these parameters are practical. The sunspot number, as a monthly value, cannot be used for hourly $\alpha_o$ determinations. The carbon ratio, while useful, again relies upon SWICS measurements which may not be available. The fit of the $O^{7+}$ abundance to solar wind speed in the first panel of Figure 3 (middle row) is shown in equation (16), which combined with equation (15) provides two components (with a combined error) of the three required to calculate $\alpha_o$ from the incoming solar wind speed alone. We then calculate the O/H ratio from the solar wind speed. As the spread of fits is wider than in the previous fittings we find the median of each 10 km/s speed bin and fit these points, thus reducing the effect of outliers on the fitting. The fit equation is shown in equation (17) and plotted in the third panel of Figure 3 (middle row).

**Table 1.** Table of Example Oxygen Parameters With Solar Wind Speed[a]

| $v$ (km/s) | $O^{7+}$ | $O^{8+}$ | O/H [b]($\times 10^{-4}$) | O/H [c]($\times 10^{-4}$) | $\alpha_o$ [b]($\times 10^{-17}$) |
|---|---|---|---|---|---|
| 200 | 0.4675 | 0.0622 | 0.127 | 1.65 | 1.301 |
| 250 | 0.2941 | 0.0252 | 0.831 | 1.65 | 5.570 |
| 300 | 0.2014 | 0.0120 | 1.488 | 1.65 | 7.270 |
| 350 | 0.1462 | 0.0064 | 2.097 | 1.65 | 7.971 |
| 400 | 0.1108 | 0.0037 | 2.660 | 1.65 | 8.210 |
| 450 | 0.0868 | 0.0023 | 3.174 | 1.65 | 7.960 |
| 500 | 0.0697 | 0.0015 | 3.642 | 4.37 | 7.614 |
| 550 | 0.0572 | 0.0010 | 4.063 | 4.37 | 7.227 |
| 600 | 0.0477 | 0.0007 | 4.436 | 4.37 | 6.827 |
| 650 | 0.0404 | 0.0005 | 4.762 | 4.37 | 6.254 |
| 700 | 0.0347 | 0.0004 | 5.040 | 4.37 | 5.720 |
| 750 | 0.0300 | 0.0003 | 5.272 | 4.37 | 5.226 |
| 800 | 0.0263 | 0.0002 | 5.456 | 4.37 | 4.769 |
| 850 | 0.0232 | 0.0002 | 5.593 | 4.37 | 4.345 |
| 900 | 0.0206 | 0.0001 | 5.682 | 4.37 | 3.952 |
| 950 | 0.0184 | 0.0001 | 5.725 | 4.37 | 3.588 |
| 1000 | 0.0166 | 0.0001 | 5.720 | 4.37 | 3.249 |

[a]These parameters are calculated from equations (15)–(17). $\alpha_o$ is calculated from equation (2), using these oxygen parameters.
[b]Solar wind velocity dependent.
[c]Fast and slow wind values only.

The results for solar wind speeds ranging from 200 to 1000 km/s are given in Table 1; the relevant $O^{7+}$, $O^{8+}$, and O/H values are also included. Column 5 of Table 1 also includes the modal fast/slow O/H ratio for reference. Splitting up the data into 50 km/s bins, we took the standard deviation of each oxygen input from the fit to provide $\alpha_o$ error estimates, providing an uncertainty factor of 2.2. It should be noted that this error relies on the combination of standard deviations from each fit and hence dependent on the number of data points in each bin.

$$O_{7+} = 28120 \times v^{-2.077} \tag{16}$$

$$O/H = -3.16 \times 10^{-4} + 1.83 \times 10^{-6} v - 9.45 \times 10^{-10} v^2 \tag{17}$$

where $v$ is the solar wind speed in kilometer per second.

As well as finding solar wind $\alpha_o$ values, Table 1 can be used to provide all the inputs for calculating $\alpha_o$ around the magnetopause, the only difference in this situation being the lower bulk flow speed and increased thermal velocity.

## 6. Conclusions

We have compared empirical oxygen values, for $O^{7+}$, $O^{8+}$, and O/H to those measured by ACE over a 13 year period. This has included a comparison of calculated efficiency values, known as $\alpha_{O^{7,8+}}$, for X-ray charge exchange emission. Splitting the data into slow and fast solar wind values provided binned modal $O^{7+}$ abundances of 8.9% and 1.6%, respectively. The $O^{8+}$ abundances had a binned modal peak at 0%, although examination of individual data points provides median abundances of 0.44% and 0.12% for slow and fast solar wind speeds, respectively. The O/H ratio returned modal peaks of $1.65 \times 10^{-4}$ and $4.37 \times 10^{-4}$, for slow and fast solar wind, which agrees well with previous experimentally determined values.

To provide better estimates of SWCX in planetary environments, we fit the three main parameters as a function of solar wind speed, allowing an approximate $\alpha_{O^{7,8+}}$ value to be calculated using only limited solar wind data. These calculated $\alpha_{O^{7,8+}}$ values are included along with the respective $O^{7+}$, $O^{8+}$, and O/H values for a range of solar wind speeds in Table 1. The relevant fit equations are shown in equations (15)–(17) and are valid in both

the solar wind and the planetary environment, allowing the oxygen based $\alpha$ value in the 0.5–0.7 keV energy band to be determined for planetary charge exchange emission with neutral hydrogen.

It is also of interest to note that at the modal solar wind velocity of 350 km/s (Figure 2e), $\alpha_{O^{7,8+}}$ is $\sim 10^{-16}$ eV cm$^2$, a factor of 6 times lower than the all species $\alpha$ value. The narrow 0.5–0.7 keV energy band contains relatively few line emission contributions in comparison to SWCX spectral models in the full 0.3–0.85 keV range, 5 compared to 33 [*Carter et al.*, 2010]. As there are just over 6 times as many emission lines in the empirical $\alpha$, the value of $6 \times 10^{-16}$ for all species, while unable to vary with solar wind compositional changes, is a reasonable average value.

**Acknowledgments**
The authors gratefully acknowledge Jennifer Carter for assistance with the manuscript preparation. The ACE solar wind composition data (level 2) were taken from the ACE Science Center www.srl.caltech.edu/ACE/ASC/. The monthly sunspot data have been sourced from the WDC-SILSO, Royal Observatory of Belgium, Brussels. This research used the SPECTRE High Performance Computing Facility at the University of Leicester. Effort sponsored by the Air Force Office of Scientific Research, Air Force Material Command, USAF, under grant FA9550-14-1-0200 is acknowledged. The U.S. government is authorized to reproduce and distribute reprints for Governmental purposes notwithstanding any copyright notation thereon.

## References

Bodewits, D. (2007), Cometary X-rays. Solar wind charge exchange in cometary atmospheres, PhD thesis, Univ. of Groningen.
Burlaga, L. F., and A. J. Lazarus (2000), Lognormal distributions and spectra of solar wind plasma fluctuations: Wind 1995–1998, *J. Geophys. Res.*, *105*(A2), 2357–2364, doi:10.1029/1999JA900442.
Carter, J. A., S. Sembay, and A. Read (2010), A high charge state coronal mass ejection seen through solar wind charge exchange emission as detected by XMM-Newton, *Mon. Not. R. Astron. Soc.*, *402*, 867, doi:10.1111/j.1365-2966.2009.15985.x.
Carter, J. A., S. Sembay, and A. Read (2011), Identifying XMM-Newton observations affected by solar wind charge exchange—Part II, *Astron. Astrophys.*, *527*, A115, doi:10.1051/0004-6361/201015817.
Collier, M. R., T. E. Moore, M.-C. Fok, B. Pilkerton, S. Boardsen, and H. Khan (2005), Low energy neutral atom signatures of magnetopause motion in response to southward $B_z$, *J. Geophys. Res.*, *110*, A02102, doi:10.1029/2004JA010626.
Collier, M. R., et al. (2012), Prototyping a global soft X-ray imaging instrument for heliophysics, planetary science, and astrophysics science, *Astron. Nachr.*, *333*(4), 378–382, doi:10.1002/asna.201211662.
Collier, M. R., et al. (2014), On lunar exospheric column densities and solar wind access beyond the terminator from ROSAT soft X-ray observations of solar wind charge exchange, *J. Geophys. Res. Planets*, *119*, 1459–1478, doi:10.1002/2014JE004628.
Cravens, T. E. (1997), Comet Hyakutake x-ray source: Charge transfer of solar wind heavy ions, *Geophys. Res. Lett.*, *24*(1), 105–108, doi:10.1029/96GL03780.
Cravens, T. E. (2000), Heliospheric X-ray emission associated with charge transfer of the solar wind with interstellar neutrals, *Astrophys. J.*, *532*(2), L153, doi:10.1086/312574.
Cravens, T. E., I. P. Robertson, and S. L. Snowden (2001), Temporal variations of geocoronal and heliospheric X-ray emission associated with the solar wind interaction with neutrals, *J. Geophys. Res.*, *106*(A11), 24,883–24,892, doi:10.1029/2000JA000461.
Dennerl, K. (2008), X-rays from Venus observed with Chandra, *Planet. Space Sci*, *56*(10), 1414–1423, doi:10.1016/j.pss.2008.03.008.
Geiss, J., G. Gloeckner, and R. von Steiger (1995), Origin of the solar wind from composition data, *Space Sci. Rev.*, *72*, 49–60.
Gloeckler, G., et al. (1998), Investigation of the composition of solar and interstellar matter using solar wind and pick up ion measurements with SWICS and SWIMS on the ACE spacecraft, *Space Sci. Rev.*, *86*, 497–539, doi:10.1023/A:1005036131689.
Hefti, S., H. Grünwaldt, P. Bochsler, and M. R. Aellig (2000), Oxygen freeze-in temperatures measured with SOHO/CELIAS/CTOF, *J. Geophys. Res.*, *105*(A5), 10,527–10,533, doi:10.1029/1999JA900384.
Holmström, M., S. Barabash, and E. Kallio (2001), X-ray imaging of the solar wind–Mars interaction, *Geophys. Res. Lett.*, *28*(7), 1287–1290, doi:10.1029/2000GL012381.
Hundhausen, A. J., H. E. Gilbert, and S. J. Bame (1968), Ionization state of the interplanetary plasma, *J. Geophys. Res.*, *73*(17), 5485–5493, doi:10.1029/JA073i017p05485.
Ishikawa, K., Y. Ezoe, Y. Miyoshi, N. Terada, K. Mitsuda, and T. Ohashi (2013), Suzaku observation of strong solar-wind charge-exchange emission from the terrestrial exosphere during a geomagnetic storm, *Publ. Astron. Soc. Jpn.*, *65*(3), 63, doi:10.1093/pasj/65.3.63.
Kuntz, K. D., Y. M. Collado-Vega, M. R. Collier, H. K. Connor, T. E. Cravens, D. Koutroumpa, F. S. Porter, I. P. Robertson, D. G. Sibeck, and S. L. Snowden (2015), The solar wind charge-exchange production factor for hydrogen, *Astrophys. J.*, *808*(2), 143, doi:10.1088/0004-637X/808/2/143.
Lepri, S. T., E. Landi, and T. H. Zurbuchen (2013), Solar wind heavy ions over solar cycle 23: ACE/SWICS measurements, *Astrophys. J.*, *768*, 94, doi:10.1088/0004-637x/768x1/94.
Lisse, C. M., et al. (1996), Discovery of X-ray and extreme ultraviolet emission from comet C/Hyakutake 1996 B2, *Science*, *274*(5285), 205–209, doi:10.1126/science.274.5285.205.
Lisse, C. M., et al. (2005), Chandra observations of comet 2P/Encke 2003: First detection of a collisionally thin, fast solar wind charge exchange system, *Astrophys. J.*, *635*, 1329–1347.
McComas, D. J., et al. (1998), Ulysses' return to the slow solar wind, *Geophys. Res. Lett.*, *25*(1), 1–4.
Ogasawara, K., V. Angelopoulos, M. A. Dayeh, S. A. Fuselier, G. Livadiotis, D. J. McComas, and J. P. McFadden (2013), Characterizing the dayside magnetosheath using energetic neutral atoms: IBEX and THEMIS observations, *J. Geophys. Res. Space Physics*, *118*, 3126–3137, doi:10.1002/jgra.50353.
Pepino, R., V. Kharchenko, A. Dalgarno, and R. Lallement (2004), Spectra of the X-ray emission induced in the interaction between the solar wind and heliospheric gas, *Astrophys. J.*, *617*(2), 1347–1352.
Robertson, I. P., and T. E. Cravens (2003), X-ray emission from the terrestrial magnetosheath, *Geophys. Res. Lett.*, *30*(8), 1439, doi:10.1029/2002GL016740.
Robertson, I. P., M. R. Collier, T. E. Cravens, and M.-C. Fok (2006), X-ray emission from the terrestrial magnetosheath including the cusps, *J. Geophys. Res.*, *111*, A12105, doi:10.1029/2006JA011672.
Schwadron, N. A., and T. E. Cravens (2000), Implications of solar wind composition for cometary X-rays, *Astrophys. J.*, *554*, 558–566.
Tracy, P. J., J. C. Kasper, T. H. Zurbuchen, J. M. Raines, P. Shearer, and J. Gilbert (2015), Thermalization of heavy ions in the solar wind, *Astrophys. J.*, *812*(2), 170, doi:10.1088/0004-637X/812/2/170.
von Steiger, R., and T. H. Zurbuchen (2011), Polar coronal holes during the past solar cycle: Ulysses observations, *J. Geophys. Res.*, *116*, A01105, doi:10.1029/2010JA015835.
von Steiger, R., T. H. Zurbuchen, and D. J. McComas (2010), Oxygen flux in the solar wind: Ulysses observations, *Geophys. Res. Lett.*, *37*, L22101, doi:10.1029/2010GL045389.
Webb, D. F., and R. A. Howard (1994), The solar cycle variation of coronal mass ejections and the solar wind mass flux, *J. Geophys. Res.*, *99*(A3), 4201–4220, doi:10.1029/93JA02742.

Whittaker, I. C., S. Sembay, J. A. Carter, A. M. Read, S. E. Milan, and M. Palmroth (2016), Modeling the magnetospheric X-ray emission from solar wind charge exchange with verification from XMM-Newton observations, *J. Geophys. Res. Space Physics*, *121*, 4158–4179, doi:10.1002/2015JA022292.

Zurbuchen, T. H., and I. G. Richardson (2006), In-situ solar wind and magnetic field signatures of interplanetary coronal mass ejections, *Space Sci. Rev.*, *123*(1), 31–43, doi:10.1007/s11214-006-9010-4.

Zurbuchen, T. H., L. A. Fisk, G. Gloeckler, and R. von Steiger (2002), The solar wind composition throughout the solar cycle: A continuum of dynamic states, *Geophys. Res. Lett.*, *29*(9), 1352, doi:10.1029/2001GL013946.